Vysoké učení technické v Brně
Brno University of Technology

Fakulta strojního inženýrství
Faculty of mechanical engineering

Ústav matematiky
Institute of mathematics

Ing. Marek Pivovarník

New Approaches in Airborne Thermal Image Processing for Landscape Assessment

Nové přístupy zpracování leteckých obrazových termálních dat k hodnocení krajiny

zkrácená verze dizertační práce

Studijní obor: Aplikovaná matematika
Vedoucí práce: doc. Ing. Mgr. František Zemek, Ph.D.

Klíčová slova

Dálkový průzkum Země, letecké obrazové data, termální hypespektrální data, separace teploty a emisivity, TASI senzor, algoritmus, tepelné záření.

Key words

Remote sensing, airborne image data, thermal hyperspectral data, temperature and emissivity separation, TASI sensor, algorithm, thermal infrared.

Místo uložení disertační práce

Areálová knihovna Fakulty strojního inženýrství VUT v Brně

ISBN 80-214-
ISSN 1213-4198

Obsah

Introduction

Airborne thermal hyperspectral data offer valuable information about the observed objects. Image data of this kind has found application in fields focused on evapotranspiration [27], vegetation [28], soil moisture [31], mineral mapping [26] and urban studies [34]. Let us emphasize that the most important quantities derived form airborne thermal hyperspectral data are temperature and emissivity. However, direct derivation of temperature and emissivity by observing radiance in N bands results in N equations but $N+1$ unknowns (N emissivities plus temperature). This problem, separating the contributions of temperature and emissivity to observed radiances, has been the subject of a great deal of research and many methods have been developed to address it [23].

The temperature and emissivity separation algorithm [14], designated TES, that was developed for the Advanced Spaceborne Thermal Emission and Reflection Radiometer (ASTER), has since been applied to processing of TIR image data acquired by various airborne and spaceborne, and various multispectral and hyperspectral sensors.

Section 2 describes the problem of temperature and emissivity separation and Section 3 introduces the improvement of the TES algorithm, which is referred to as Optimized Smoothing for Temperature and Emissivity Separation (OSTES). The OSTES algorithm is firstly tested on a set of simulated data representing different natural materials as they would be acquired by Thermal Airborne Spectrographic Imager (TASI) sensor. Section 4 includes incorporation of the OSTES algorithm to the processing chain of image data acquired by the TASI sensor and then it compares the performance of the OSTES and TES algorithms on image data obtained from TASI.

Aims of dissertation

- Enhancing the accuracy and precision of the products generated by the TES algorithm.
- Incorporating a new algorithm to the processing chain applied on image data acquired by TASI sensor.

1. Background

Imaging systems

From the wide range of airborne sensors operating in the TIR region one are chosen to analyze the performance of the OSTES algorithm: TASI sensor developed by Itres Ltd. (Calgary, Canada).

The TASI sensor is one of the very few commercially available hyperspectral TIR sensors. It contains 32 bands all of which are in the TIR region. Bands are situated in the 8 to 11.5 μm region and have a Full Width at Half Maximum FWHM $\approx 0.11\,\mu$m with Noise Equivalent Temperature difference NEΔT ≈ 0.1 K. The response function of this sensor is depicted in Fig. 1.

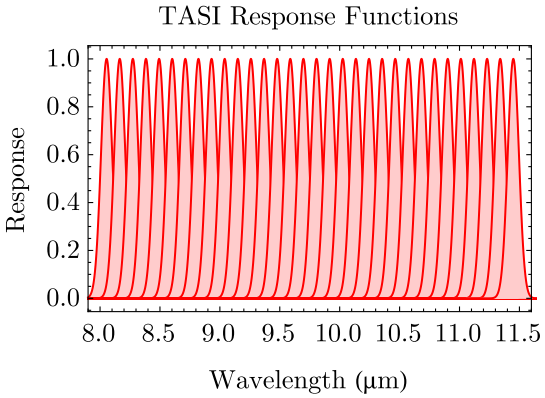

Figure 1: Response functions of TASI sensor.

Theoretical Basis

Any TIR sensor observing the earth from an airborne or spaceborne platform receives radiation from the surface, attenuated by atmosphere, plus radiation from the atmosphere along the line of sight. Thus the measured radiance at sensor level (L_m) consists mainly of radiance emitted from the land surface, downwelling atmospheric radiance ($L^{\downarrow}_\mathrm{atm}$) reflected by the surface and the atmospheric upwelling radiance ($L^{\uparrow}_\mathrm{atm}$). The sum of all these components is expressed by a radiative transfer equation (RTE) as follows:

$$L_\mathrm{m} = \tau\varepsilon B(T_\mathrm{s}) + \tau(1-\varepsilon)L^{\downarrow}_\mathrm{atm} + L^{\uparrow}_\mathrm{atm}, \tag{1}$$

where $B(T_\mathrm{s})$ is radiance of the surface at temperature T_s according to the Planck's law, ε is the surface's emissivity and τ is atmospheric transmittance. The RTE as applied to thermal remote sensing is discussed at length

in [23]. It is important to emphasize that all elements in the equation are wavelength dependent but notation for this is omitted for the sake of clarity.

Since sensors are of finite bandwidth, quantities in eq. (1) are replaced by band-effective equivalents. These are obtained using weighted averages:

$$X_i = \frac{\int_{\lambda_1}^{\lambda_2} r_i(\lambda) X(\lambda)\,\mathrm{d}\lambda}{\int_{\lambda_1}^{\lambda_2} r_i(\lambda)\,\mathrm{d}\lambda}, \tag{2}$$

where $r_i(\lambda)$ is response function of band i, λ_1 and λ_2 are lower and upper boundaries of band i and any quantity can be substituted for X.

For any multispectral or hyperspectral sensor with N bands one gets an equation in the form of eq. (1) for each band. Even after compensating for the atmosphere the system of N equations contains N unknown emissivities plus an unknown temperature, which is considered to be constant in all spectral bands. This makes the system of equations underdetermined.

2. TES Algorithm

Many approaches have been developed to overcome the problem of having an underdetermined system of equations [23]. Among these, the TES algorithm is the most popular and it is widely applied to many sensors including TASI. Application of TES to data acquired by the TASI sensor is mentioned in a few studies [35, 27].

The TES algorithm is based on a semi-empirical relationship between spectral contrast (i.e. difference between the highest and lowest values in the emissivity spectrum) and the minimum emissivity. The algorithm consists of three modules, namely the Normalization Emissivity Module (NEM) [12], the Ratio module and the Maximum-Minimum Difference (MMD) module [24]. The inputs to the algorithm are land-leaving radiance L_{LL} and downwelling radiance $L^{\downarrow}_{\mathrm{atm}}$. Land-leaving radiance is obtained from eq. (1) by compensating for atmospheric transmissivity τ and atmospheric upwelling radiance $L^{\uparrow}_{\mathrm{atm}}$:

$$L_{\mathrm{LL}} = \varepsilon B(T_{\mathrm{s}}) + (1-\varepsilon) L^{\downarrow}_{\mathrm{atm}}. \tag{3}$$

The NEM module performs an iterative process for estimating temperature and emissivity, and compensating for the downwelling radiance. The output of the NEM module is an initial estimation of temperature and

emissivity. Then the ratio module normalizes the emissivities obtained by the NEM module by their arithmetic mean. Thus one obtains the so called β spectrum, which should be less sensitive to sensor noise. Finally, the maximum and minimum of the β spectrum are found and their difference (MMD) is used in following semi-empirical relationship:

$$\varepsilon_{\min} = 0.994 - 0.687 \times \mathrm{MMD}^{0.737}. \quad (4)$$

Derivation of eq. (4) is explained in following paragraph. Ratioing the β spectrum back to an emissivity spectrum with knowledge of minimum emissivity increases the precision of the emissivity spectrum estimates. The band with highest emissivity is then used for temperature estimation.

The relationship between spectral contrast and minimum emissivity, shown in eq. (4), is a regression based on 86 laboratory spectra of rocks, soils, vegetation, snow and water chosen from the ASTER spectral library [5]. It is important to note that eq. (4) is tailored for the ASTER sensor. To apply TES to a different sensor, the regression of $\varepsilon_{\min}$ on MMD must be refined by using sensor specific response functions.

The regression coefficients in eq. (4) were recomputed for TASI sensor using their respective response functions. The regression was performed on a set of 108 spectra chosen from same categories and library as in the ASTER case mentioned above. The coefficients for TASI sensor are following:

$$\varepsilon_{\min} = 1.001 - 0.737 \times \mathrm{MMD}^{0.760}. \quad (5)$$

After ASTER was launched, [15] and [29] suggested to replace the power regression shown in eq. (4) with linear regression. The replacement is connected with modification of the threshold for separating materials with low spectral contrast. The main advantage is elimination of artefacts in retrievals. However, the drawback is loss of accuracy in cases of materials with low spectral contrast [29]. The TES algorithm used for generation ASTER standard products [4], as well as its modifications for other sensors [33, 20, 35, 32, 21, 18, 25, 19], is based on the power law regression. Thus, in this work the TES algorithm is considered to be that using the power regression.

3. Algorithm Improvement

The algorithm described below brings a new approach for separating temperature and emissivity by replacing the NEM module in the TES algo-

rithm with a completely new module. The new module is based on the similarity between brightness temperature spectral features and emissivity spectral features. Brightness temperature is obtained from land-leaving radiance under the assumption of emissivity $\varepsilon = 1$ for every wavelength. Although land-leaving radiance includes some portion of reflected downwelling radiance, it still retains the spectral features arising from the emissivity of the surface materials, which is 0.6 or higher for natural materials [14]. Since the magnitude of downwelling radiance is usually much lower than the surface radiance the features contained in the brightness temperature spectra may be distorted but will not be completely hidden. The new module approximates this relation between brightness temperature T_b and emissivity. The OSTES deeply discussed in [1].

In order to demonstrate the relationship, three emissivity samples with different spectral contrasts were chosen from the ASTER spectral library, namely green grass, fine sandy loam and altered volcanic tuff. These emissivities are depicted in Figure 2 (solid lines) together with corresponding band-effective values for TASI sensor (empty symbols). Band-effective values of emissivity for each sensor are distributed among three samples for reasons of clarity. These emissivities were applied to Planck's law at temperature 300 K and combined with downwelling radiance from standard mid-latitude summer atmosphere generated by MODerate resolution atmospheric TRANsmission (MODTRAN) [6]. The resulting radiances, were transformed to band-effective quantities with respect to the TASI response function. Brightness temperatures for every band of each sensor were obtained by applying inverse Planck's law on sample land-leaving radiances under the assumption of $\varepsilon = 1$. Figure 2 also includes brightness temperatures (full symbols) in order to demonstrate spectral similarity with emissivity. Figure 3 plots emissivity against brightness temperature for chosen samples and for TASI sensor (empty symbols). These quantities clearly exhibit relationship with linear trend regardless of spectral contrast. Also displayed in Figure 3 are lines that approximate this relationship, derived in the manner described later in the next.

The only factor which can jeopardize the linear relationship between brightness temperature and emissivity is the high magnitude of downwelling radiance in comparison with surface radiance. This will occur rarely, if at all, as described in the first paragraph of this section. Let us emphasise that the brightness temperature and emissivity relationship can be approximated by the linear relationship at any surface temperature

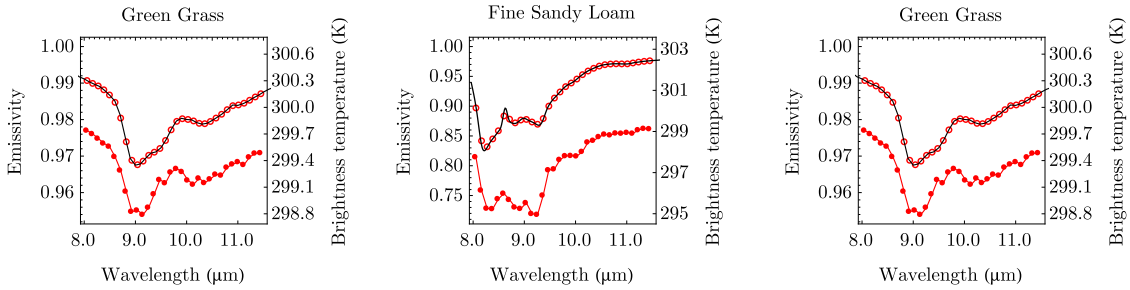

(a) Case I **(b)** Case II **(c)** Case III

Figure 2: Emissivity spectra (black solid line) of three samples chosen from ASTER spectral library [5]. Symbols represent band-effective values of emissivity (empty symbols) and brightness temperature (full symbols) for TASI sensor.

since we are interested in the brightness temperature features rather than in absolute values. The algorithm description below uses band-effective values of quantities linked to i-th band by subscript index i.

The dependence of emissivity ε_i on brightness temperature T_{b_i} will be approximated by following equation:

$$\varepsilon_i = pT_{\mathrm{b}_i} + q, \tag{6}$$

where p and q are empirical coefficients. These coefficients are determined by solving the system of two equations using two points, namely maximum brightness temperature coupled with emissivity equal to 1 and minimum brightness temperature coupled with lowest emissivity $\varepsilon_{\min}$:

$$\begin{aligned} 1 &= p\max(T_{\mathrm{b}_i}) + q, \\ \varepsilon_{\min} &= p\min(T_{\mathrm{b}_i}) + q. \end{aligned} \tag{7}$$

The next step is estimation of the the lowest emissivity $\varepsilon_{\min}$.

This is done by varying $\varepsilon_{\min}$ over the range of possible emissivities for natural materials $[0.6, 1]$, determining corresponding coefficients p and q by solving eq. (7) and then approximating emissivity by eq. (6) using brightness temperature for all spectral bands. The estimated emissivity is then used together with land-leaving radiance L_{LL} and downwelling radiance $L^{\downarrow}$ in a computation that yields spectral radiance:

$$L'_i = \frac{L_{\mathrm{LL}_i} - (1-\varepsilon_i)L_i^{\downarrow}}{\varepsilon_i}. \tag{8}$$

The temperature in every spectral band is derived from spectral radiance L' applying inverse Planck's law. The highest one is chosen as the reference

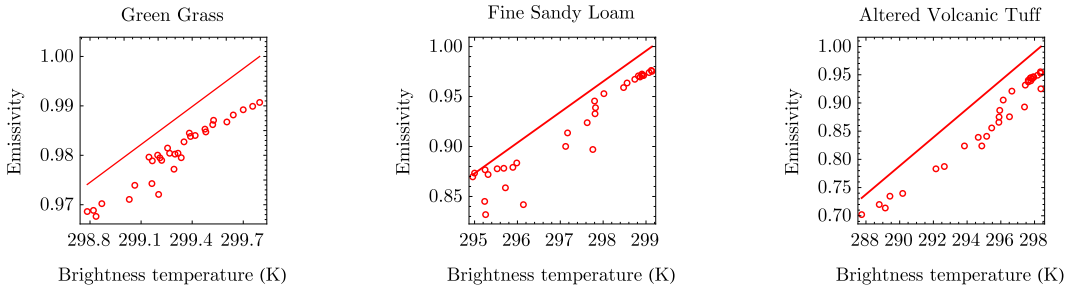

(a) Case I **(b)** Case II **(c)** Case III

Figure 3: Symbols represent examples of the relationship between brightness temperature T_b and emissivity as would be observed by the TASI sensor. Lines illustrate the approximations of the relationship between brightness temperature and emissivity. The procedure used for estimation of the brightness temperature and emissivity relationship is described in the text.

temperature T_max. Finally, the estimated spectral radiance L' and Planck's law at the reference temperature T_max are normalized and compared against each other as follows:

$$\sum_i \left| \frac{B_i(T_\mathrm{max})}{||B(T_\mathrm{max})||_1} - \frac{L'_i}{||L'||_1} \right|. \tag{9}$$

The value of ε_min is considered final if its corresponding spectral radiance L' is the best fit to Planck's law.

The whole process of determining ε_min can be understood as smoothing the spectrum by finding the optimal value of ε_min. Pseudocode depicted in Figure 4 summarizes the above described procedure as a function $\textsc{SmoothingErr}(\varepsilon_\mathrm{min}, L_\mathrm{LL}, L^{\downarrow})$ evaluating the error between Planck's law and estimated spectral radiance. This function is minimized with respect to the variable ε_min as follows:

$$\underset{\varepsilon_\mathrm{min} \in [0.6,1]}{\arg\min}\ \textsc{SmoothingErr}(\varepsilon_\mathrm{min}, L_\mathrm{LL}, L^{\downarrow}). \tag{10}$$

Continuous curves in Figure 3 show the optimal brightness temperature and emissivity relationship approximation. Let us emphasize that by applying emissivities obtained from the approximated relationship between brightness temperature and emissivity to eq. (8), one gets L' as the best fit to Planck's law. This means that $B^{-1}(L'_i)$ produces a temperature value for each band. These temperatures have minimum variability since they are derived from the best fit to Planck's law. Let us also remind the reader

Function SMOOTHINGERR($\varepsilon_{\min}, L_{\mathrm{LL}}, L^{\downarrow}$)

1. $T_{\mathrm{b}_i} = B^{-1}(L_{\mathrm{LL}_i})$
2. Find p and q by solving
   $1 = p \max(T_{\mathrm{b}_i}) + q$
   $\varepsilon_{\min} = p \min(T_{\mathrm{b}_i}) + q$
3. Estimate emissivity
   $\varepsilon_i = p\, T_{\mathrm{b}_i} + q$
4. Estimate spectrum
   $L'_i = \frac{L_{\mathrm{LL}_i} - (1-\varepsilon_i) L_i^{\downarrow}}{\varepsilon_i}$
5. $T_{\max} = \max(B^{-1}(L'_i))$
6. **return**
   $\sum_i \left| \frac{B_i(T_{\max})}{||B(T_{\max})||_1} - \frac{L'_i}{||L'||_1} \right|$

Figure 4: Pseudocode of the function that is being minimized in order to estimate the value of $\varepsilon_{\min}$.

that maximum brightness temperature is coupled with emissivity equal to 1, which implies that it is part of the set of temperatures with smallest variability. It is important to note that maximum brightness temperature T_{b} computed from land-leaving radiance is usually less than surface temperature T computed from surface radiance. Land-leaving radiance is less than surface radiance since natural materials are of emissivity higher than 0.6 and the contribution from reflected downwelling radiance is usually much lower than surface radiance. By reason of maximum brightness temperature T_{b} being less than surface temperature T and by being part of the set of temperatures with smallest variability, it can be concluded that maximum temperature from the set of temperatures tends to be the closest to the surface temperature T and is therefore taken as the reference one.

Before passing emissivity to the Ratio and MMD modules, it is recomputed according to eq. (11):

$$\varepsilon_i = \frac{L_{\mathrm{LL}_i} - L_i^{\downarrow}}{B_i(T) - L_i^{\downarrow}}, \tag{11}$$

where T is the maximum temperature associated with optimal $\varepsilon_{\min}$. Equation (11) is derived from eq. (3) and it is important for relating temperature and emissivity. This recomputation keeps temperature and emissivity consistent with each other (i.e. the same temperature can be derived from any emissivity band). The emissivity is then further processed with the Ratio and MMD modules, with minor changes to the original version of the TES algorithm as it is described in [14] and [13]. These changes in-

clude: 1) there is no refinement of $\varepsilon_{\max}$ according to the emissivity spectral contrast, 2) the threshold T_1 for separation emissivities with small spectral contrast is not applied, and 3) the number of MMD iterations is set to one. Let us emphasize that before reporting algorithm outputs, emissivity is recomputed by eq. (11) using the final value of temperature.

4. OSTES validation

The OSTES algorithm was tested on both synthetic and real data. Synthetic data were generated from spectral and climatological libraries such that they cover many possible scenes and conditions. These data were simulated as would be acquired with TASI sensor. The OSTES was further tested on a real data. For this purpose image data TASI image data over urban areas of city of Brno were chosen.

Synthetic data

A data set of 6588 samples was artificially created to compare the performance of the TES and OSTES algorithms. Samples include 108 different natural surfaces chosen from ASTER spectral library [5] at different temperatures coupled with 61 different atmospheric conditions taken from TIGR (TOVS Initial Guess Retrieval) database [9, 8]. Sample temperatures range from 244 K to 310 K. In order to simulate real conditions, every sample at a certain temperature is coupled with a certain type of atmosphere. The chosen atmospheres represent a variety of possible conditions within polar, mid-latitude and tropical airmasses. These samples were processed to land-leaving and downwelling radiance, as standard TES algorithm input, and they were transformed to band-effective quantities with respect TASI response functions. Samples were passed to the algorithms individually.

The version of the original TES algorithm in cases of TASI sensor was implemented in a manner similar to that described in [20]. In addition, the implementation omits the $\varepsilon_{\max}$ refinement for emissivities with low spectral contrast. The OSTES was applied to TASI data as it is described in Section 3.

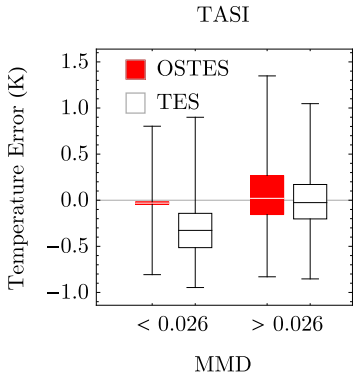

Figure 5: Box plots representing temperature error produced by OSTES and TES algorithms for TASI sensor. Results are divided in two groups based on the Maximum-Minimum emissivity Difference (MMD) in order to demonstrate the improvement of the OSTES algorithm. Whiskers represent minimum and maximum of temperature error.

Samples were passed to the TES and OSTES algorithms and the temperature and emissivity results were compared with true values. We divide the results into two groups according to the emissivity spectral contrast. We determined a threshold for Maximum-Minimum emissivity Difference (MMD) in order to separate the samples with small spectral contrast such as water, vegetation, snow or samples with small particle sizes from other samples with higher spectral contrast. The performance of both algorithms was determined by subtracting retrieved temperature from true temperature value. The temperature error and chosen MMD values for TASI are shown in Figure 5.

Application to TASI image data

The OSTES algorithm was applied on image data acquired by TASI sensor and the results were compared with emissivities obtained from *in-situ* mesaurements and the TES algorithm esmissivity estiamtions.

Experiment setup

The study was performed using data acquired over the city of Brno, Czech Republic (lat: 49.2, lon: 16.6). The examined data are subset of a flight line crossing the city from south-west to north-east. The acquisition was performed on 4.7.2015 at 14:03 (UTC). The FLIS operated by Global Change Research Institute CAS (Brno, Czech Republic) [16] was used for this

acquisition. FLIS consists of Compact Airborne Spectrographic Imager (CASI), Shortwave infrared Airborne Spectrographic Imager (SASI) and TASI sensor. All sensors are developed by Itres Ltd. (Calgary, Canada).

In-situ measurements of urban materials were performed with Fourier transform infrared (FTIR) Spectrometer Model 102 developed by D&P Instruments (Simsbury, USA). The emissivity of measured surfaces was estimated by a spectral smoothing algorithm [17]. Emissivity spectra of water and deciduous trees were not measured but instead they were extracted from ASTER spectral library [5]. All emissivity spectra were resampled with respect to TASI response functions. The study area and locations of the *in-situ* measurements are shown in the upper part of the Figure 7.

Spectral emissivity libraries are very useful for calibration and validation purposes. Let us emphasize that there are many other spectral emissivity libraries available apart from ASTER spectral library. Notable libraries are Johns Hopkins University Spectral Library [30], Arizona State University Spectral Library [10], United States Geological Survey Spectral Library [11] and the Spectral Library of Urban Materials (SLUM) [22]. In the [2] is described a spectral emissivity library which is specifically focused on spoil substrates.

The OSTES implementation in the TASI processing chain

Image data acquired by the TASI sensor were radiometrically, atmospherically and gemetrically pre-processed. The result of the pre-processing is land-leaving radiance, which is the first input parameter for the OSTES and the TES algorithm. The second input parameter to both algorithms is downwelling atmospheric radiance. This quantity was obtained from the radiative transfer model MODTRAN [6]. MODTRAN requires temperature and water vapour profiles, which were extracted from MOD07_L2 product [7] generated from MODIS image data.

The described procedure of temperature and emissivity estimation from pre-processed TASI image data is the continuation of the processing chain as is used at Global Change Research Institute CAS (Brno, Czech Republic). The schematic illustration of the OSTES implementation into the processing chain of the TASI image data is depicted in the Figure 6.

The processing of the TASI image data acquired during this experiment was limited to 22 spectral bands. First five and last five spectral bands

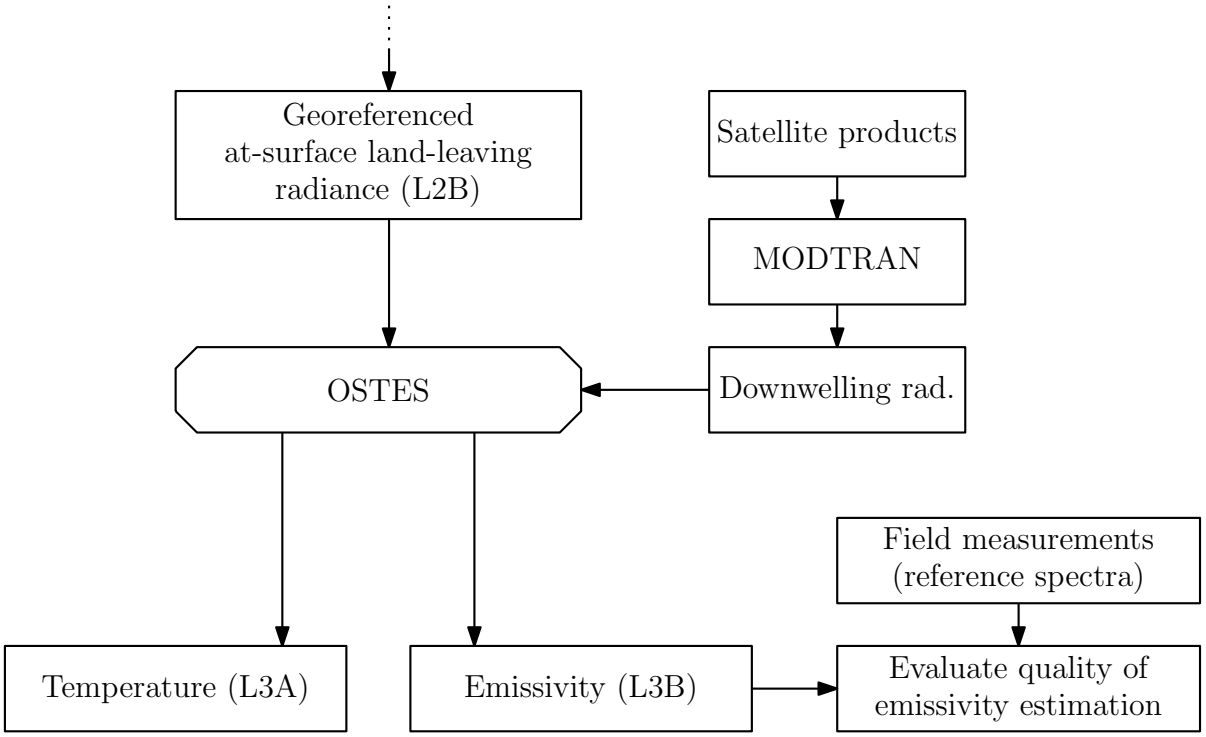

Figure 6: Continuation of the processing chain of the TASI image data. This part illustrates temperature and emissivity separation processing chain applied to the pre-processed TASI image data.

were not considered since they were most affected by imperfect atmospheric corrections.

The TASI image data were processed by the TES and OSTES algorithms in order to compare the temperature and emissivity retrievals. The TASI image data were processed with the TES algorithm by substituting OSTES algorithm in the processing chain of TASI image data. The implementation of the TES algorithm is based on the implementation described in [20] without the $\varepsilon_{\max}$ refinement for emissivities with low spectral contrast.

Comparison

Temperature and emissivity results of the OSTES algorithm are depicted in the middle and lower part of Figure 7 in the form of temperature and emissivity maps. The temperature map shows high temperature differences between vegetated and built areas. Emissivity map is a false color composition (red - band 10, green - band 15, blue - band 20) showing variability of surface materials in the image data.

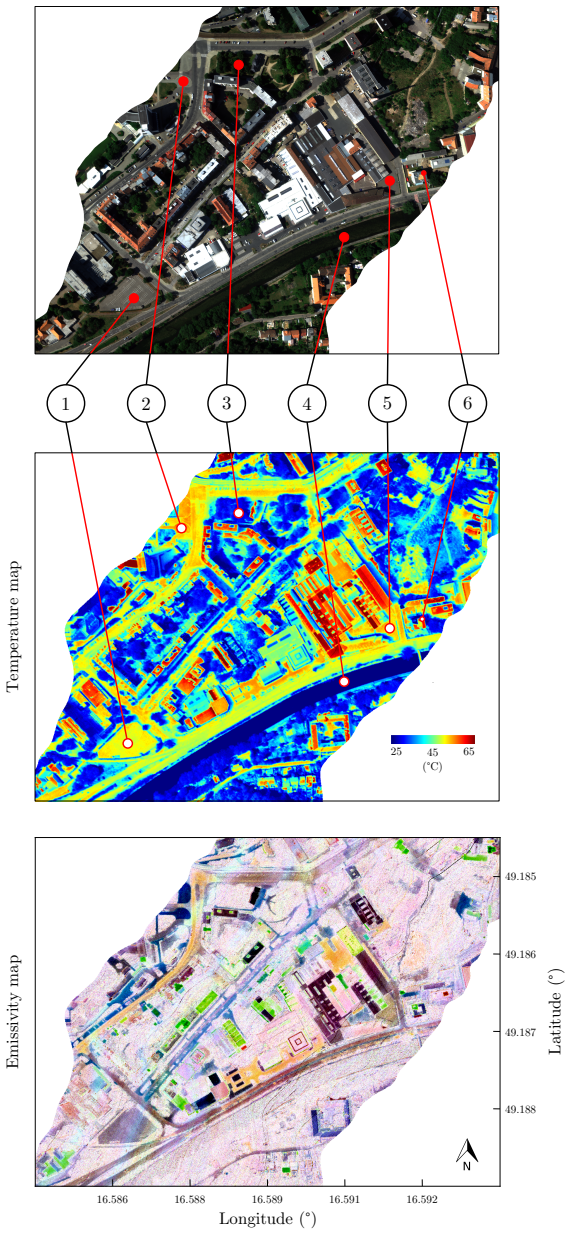

Figure 7: Part of flight line over the city of Brno. Image data were acquired on 4.7.2015 at 14:03 (UTC). The top image displays true color image of the studied area. The middle image is a temperature map obtained from the OSTES algorithm applied on image data from the TASI sensor. The bottom image is false color emissivity map obtained from OSTES algorithm (red - band 10, green - band 15, blue - band 20). On the top and middle images locations and labels of *in-situ* measurements are shown. Labels refers to following surface types: 1 - asphalt hotel parking, 2 - concrete blocks, 3 - vegetation, 4 - Svratka river, 5 - asphalt parking lots and 6 - asphalt rooftop.

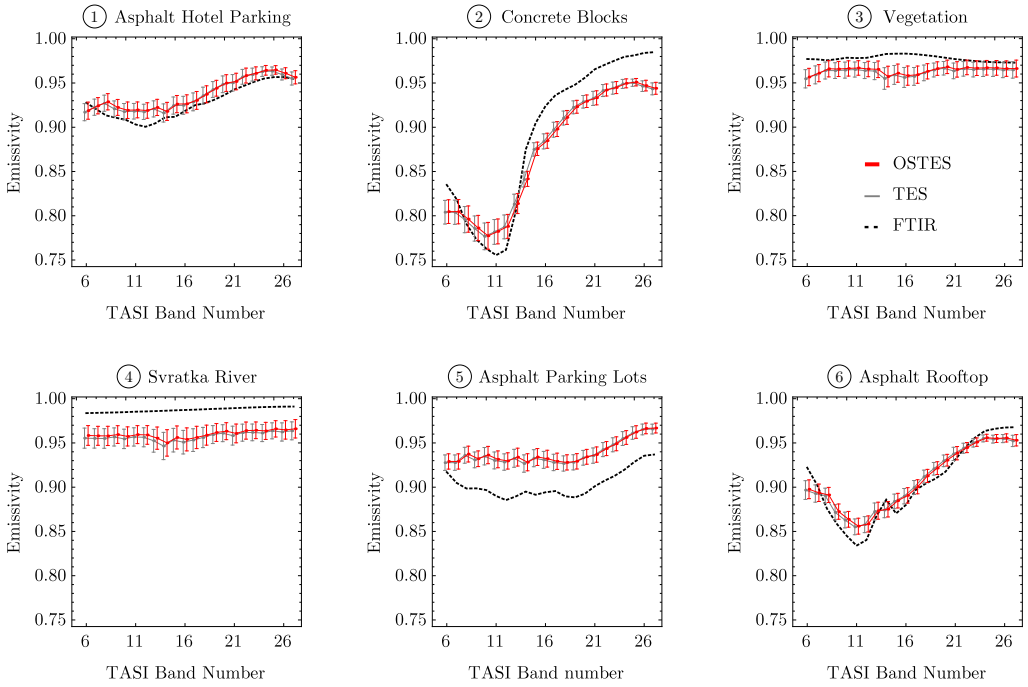

Figure 8: Comparison of TES and OSTES emissivity retrievals with emissivities obtained from *in-situ* measurements. Error bars display standard deviation.

The *in-situ* measurements were not performed during the overflight. Therefore temperature could not be used for the comparison and the validation of the TES and OSTES algorithms. The comparison of the TES and the OSTES algorithms' performance was tested against six emissivities obtained from *in-situ* measurements. Results are shown in the Figure 8, where error bars display standard deviation. Both TES and OSTES emissivity retrievals are very similar. The OSTES performs slightly better than TES in cases of deciduous trees and the river of Svratka. However, neither of these two spectra agrees with the shape and magnitude of the expected emissivity spectra. These discrepancies can be caused by various sources of errors but the main error source has been attributed to the imperfect atmospheric corrections. Emissivities of the spot 5, asphalt parking lots, retrieved by the TES and OSTES significantly differ from *in-situ* measurement. This shift in magnitude is introduced by the insufficient compensation of the downwelling radiance. This spot is surrounded by buildings, which increase the amount of downwelling radiance. This additional radiance is not included in the atmospheric parameters retrieved from MODTRAN. The rest of the emissivity retrievals are considered to follow *in-situ* measurements well. Let us emphasize the reader that OSTES

offers only moderate improvements in emissivity retrievals. These are not possible to observe in this comparison due to the magnitude of the error introduced by the imperfect atmospheric corrections.

These data were acquired within a campaign focused on detecting urban heat island of the city of Brno. The main goal was determination of parameters affecting temperatures in the city. Preliminary observations are introduced in [3].

Conclusion

Thermal hyperspectral data delivers unique information about temperature and emissivity of the Earth surface which is used in many application in both scientific and commercial fields. However, derivation of these quantities leads to the underdetermined system of equations. Many approaches have been developed to overcome this problem among which the TES algorithm is the most widely known and used.

Section 3 introduced a module that estimates temperature and emissivity from an approximation of the relationship between brightness temperature and emissivity. The new module replaces the NEM module in the original TES to create an algorithm that we call OSTES.

The performance of OSTES was firstly tested on a set of simulated data recomputed with respect to TASI response functions. Results show that temperature estimations using OSTES are more accurate and precise than TES for samples with low spectral contrast. The performance of the OSTES and TES was tested on image data acquired by TASI sensor and validated against *in-situ* measurements. The emissivity retrievals from both algorithms follow *in-situ* measurements well in most of the cases. We also conclude that improvements in atmospheric compensation will be crucial for further improvements in emissivity results. Thus, further work should be focused on this topic.

The OSTES algorithm is preferred mainly because of higher precision and accuracy under conditions of low spectral contrast. We believe that implementing OSTES to processing chain of TASI image data will benefit application for landscape assessment, as the OSTES algorithm was chosen for processing image data acquired from TASI sensor operated by Global Change Research Institute CAS (Brno, Czech Republic).

Bibliography

Author's publications

[1] PIVOVARNÍK, M., KHALSA, S.J., JIMÉNEZ-MUÑOZ, J.C., ZEMEK, F. Improved Temperature and Emissivity Separation Algorithm for Multispectral and Hyperspectral Sensors. *IEEE Transactions on Geoscience and Remote Sensing*. DOI: 10.1109/TGRS.2016.2631508. (to be published)

[2] PIVOVARNÍK, M., PIKL, M., FROUZ, J., ZEMEK, F., KOPAČKOVÁ, V., NOTESCO, G. and BEN DOR, E. A Spectral Emissivity Library of Spoil Substrates. *Data*. 2016, **1**(12). DOI: 10.3390/data1020012

[3] NOVOTNÝ, J., PIVOVARNÍK, M., KHALSA, S.J. and ZEMEK, F. Visualisation of dependencies between city structure and thermal behaviour in Brno. **In:** *23rd International Archives of the Photogrammetry, Remote Sensing and Spatial Information Sciences Congress, ISPRS 2016*. Prague, 2016, 741-745. DOI: 10.5194/isprsarchives-XLI-B2-741-2016.

Other references

[4] B. Eng, personal communication, 2015.

[5] BALDRIDGE, A.M., HOOK, S.J., GROVE, C.I. and RIVERA, G. The ASTER spectral library version 2.0. *Remote Sensing of Environment*. 2009, **113**(4), 711-715. DOI: 10.1016/j.rse.2008.11.007.

[6] BERK, A., ANDERSON, G.P., ACHARYA, P.K., BERNSTEIN, L.S., MURATOV, L., LEE, J., FOX, M., ADLER-GOLDEN, S.M., CHETWYND, J.H., HOKE, JR. M.L., LOCKWOOD, R.B., GARDNER, J.A., COOLEY, T.W., BOREL, C.C., LEWIS, P.E. and SHETTLE, E.P. MODTRAN5: 2006 update. **In:** *Algorithms and Technologies for Multispectral, Hyperspectral, and Ultraspectral Imagery XII*. Orlando (Kissimmee), FL, 2006, F2331–F2331. DOI: 10.1117/12.665077.

[7] BORBAS, E., SEEMANN, S.W., KERN, A., MOY, L., LI, J., GUMLEY, L. and MENZEL, W.P. *MODIS Atmospheric Profile Retrieval - ATBD* [online]. 2011. [cit. 2016-08-10]. Available at: http://modis-atmos.gsfc.nasa.gov/_docs/MOD07_atbd_v7_April2011.pdf

[8] CHEVALLIER, F., CHÉRUY, F., SCOTT, N.A. and CHÉDIN, A. A neural network approach for a fast and accurate computation of a longwave radiative budget. *Journal of Applied Meteorology*. 1998, **37**(11), 1385-1397. DOI: 10.1175/1520-0450(1998)037¡1385:ANNAFA¿2.0.CO;2.

[9] CHÉDIN, A., SCOTT, N.A., WAHICHE, C. and MOULINIER, P. The improved initialization inversion method: a high resolution physical method for temperature retrievals from satellites of the TIROS-N series. *Journal of*

Climate and Applied Meteorology. 1985, **24**(2), 128-143. DOI: 10.1175/1520-0450(1985)024¡0128:TIIIMA¿2.0.CO;2

[10] CHRISTENSEN, P.R., BANDFIELD, J.L., HAMILTON, V.E., HOWARD, D.A., LANE, M.D., PIATEK, J.L., RUFF, S.W. and STEFANOV, W.L. A thermal emission spectral library of rock-forming minerals. *Journal of Geophysical Research: Planets*. 2000, **105**(E4), 9735-9739. DOI: 10.1029/1998JE000624.

[11] CLARK, R.N., SWAYZE, G.A., WISE, R., LIVO, E., HOEFEN, T., KOKALY, R., SUTLEY, S.J. *USGS digital spectral library splib06a* [online]. U.S. Geological Survey, Digital Data Series 231, 2007. [cit. 2016-07-12]. Available at: http://speclab.cr.usgs.gov/spectral.lib06

[12] GILLESPIE, A.R., *Lithologic mapping of silicate rocks using TIMS* [online]. Jet Propulsion Lab., California Inst. of Tech., Pasadena, CA, United States, 1986. [cit. 2016-08-10]. Available at: http://ntrs.nasa.gov/search.jsp?R=19870007685

[13] GILLESPIE, A.R., ROKUGAWA, S., HOOK, S., MATSUNAGA, T. and KAHLE, A.B. *Temperature/Emissivity Separation Algorithm Theoretical Basis Document, Version 2.4* [online]. Pasadena: Jet Propulsion Laboratory, 1999. [cit. 2016-01-19]. Available at: http://eospso.nasa.gov/sites/default/files/atbd/atbd-ast-05-08.pdf

[14] GILLESPIE, A.R., ROKUGAWA, S., MATSUNAGA, T., COTHERN, J.S., HOOK, S. and KAHLE, A.B. A temperature and emissivity separation algorithm for Advanced Spaceborne Thermal Emission and Reflection Radiometer (ASTER) images. *IEEE Transactions on Geoscience and Remote Sensing*. 1998, **36**(4), 1113-1126. DOI: 10.1109/36.700995.

[15] GUSTAFSON, W.T., GILLESPIE, A.R. and YAMADA, G.J. Revisions to the ASTER temperature/emissivity separation algorithm. **In:** *Second Recent Advances in Quantitative Remote Sensing*. Valencia, 2006, 770-775.

[16] HANUŠ, J., FABIÁNEK, T., KAPLAN, V. and HOMOLOVÁ, L. Flying laboratory of imaging systems (FLIS) at CzechGlobe. **In:** *SGEM2014 Conference Proceedings*. 2014, 177-182. DOI: 10.5593/SGEM2014/B23/S10.022. ISBN 978-619-7105-12-4. ISSN 1314-2704.

[17] HORTON, K.A., JOHNSON, J.R. and LUCEY, P.G. Infrared Measurements of Pristine and Disturbed Soils 2. Environmental Effects and Field Data Reduction. Remote Sensing of Environment. 1998, **64**(1), 47-52. DOI: 10.1016/S0034-4257(97)00167-3.

[18] HULLEY, G. and HOOK, S.J. Generating Consistent Land Surface Temperature and Emissivity Products Between ASTER and MODIS Data for Earth Science Research. *IEEE Transactions on Geoscience and Remote Sensing*. 2011, **49**(4), 1304-1315. DOI: 10.1109/TGRS.2010.2063034.

[19] HULLEY, G. and HOOK, S.J. *HyspIRI Level-2 Thermal Infrared (TIR) Land Surface Temperature and Emissivity Algorithm Theoretical Basis Document* [online]. Pasadena, California: Jet Propulsion Laboratory, California Institute of Technology, 2011. [cit. 2016-01-19]. Available at: https://hyspiri.jpl.nasa.gov/downloads/Algorithm_Theoretical_Basis/HyspIRI_L2_Surface_Temperature_Emissivity_JPL_Pub_11-5_10102011.pdf

[20] JIMÉNEZ-MUÑOZ, J.C., SOBRINO, J.A. and GILLESPIE, A.R. Surface Emissivity Retrieval From Airborne Hyperspectral Scanner Data: Insights on Atmospheric Correction and Noise Removal. *IEEE Geoscience and Remote Sensing Letters*. 2012, **9**(2), 180-184. DOI: 10.1109/LGRS.2011.2163699.

[21] JIMÉNEZ-MUÑOZ, J.C., SOBRINO, J.A., MATTAR, C., HULLEY, G. and GOTTSCHE, F.-M. Temperature and Emissivity Separation From MSG/SEVIRI Data. *IEEE Transactions on Geoscience and Remote Sensing*. 2014, **52**(9), 5937-5951. DOI: 10.1109/TGRS.2013.2293791.

[22] KOTTHAUS, S., SMITH, T.E.L., WOOSTER, M.J. and GRIMMOND, C.S.B. Derivation of an urban materials spectral library through emittance and reflectance spectroscopy. *ISPRS Journal of Photogrammetry and Remote Sensing*. 2014, **94**, 194-212. DOI: 10.1016/j.isprsjprs.2014.05.005.

[23] LI, Z., TANG, B., WU, H., REN, H., YAN, G., WAN, Z., TRIGO, I.F. and SOBRINO, J.A. Satellite-derived land surface temperature: Current status and perspectives. *Remote Sensing of Environment* [online]. 2013, **131**, 14-37. DOI: 10.1016/j.rse.2012.12.008.

[24] MATSUNAGA, T. A Temperature-Emissivity Separation Method Using an Empirical Relationship between the Mean, the Maximum, and the Minimum of the Thermal Infrared Emissivity Spectrum. *Journal of the Remote Sensing Society of Japan*. 1994, **14**(3), 230–241. DOI: 10.11440/rssj1981.14.230

[25] MUSHKIN, A., BALICK, L.K., and GILLESPIE, A.R. Temperature/emissivity separation of MTI data using the Terra/ASTER TES algorithm. **In:** *Algorithms and Technologies for Multispectral, Hyperspectral, and Ultraspectral Imagery VIII*. Orlando, FL: SPIE, 2002, 328-337. DOI: 10.1117/12.478764.

[26] NOTESCO, G., KOPAČKOVÁ, V., ROJÍK, P., SCHWARTZ, G., LIVNE, I. and DOR, E. Mineral Classification of Land Surface Using Multispectral LWIR and Hyperspectral SWIR Remote-Sensing Data. A Case Study over the Sokolov Lignite Open-Pit Mines, the Czech Republic. *Remote Sensing*. 2014, **6**(8), 7005-7025. DOI: 10.3390/rs6087005.

[27] PIPIA, L., PEREZ, F., TARDA, A., MARTINEZ, L. and ARBIOL, R. Simultaneous usage of optic and thermal hyperspectral sensors for crop water stress characterization. **In:** *IEEE International Geoscience and Remote Sensing Symposium*. Munich: IEEE, 2012, 6661-6664. DOI: 10.1109/IGARSS.2012.6352071.

[28] RIBEIRO DA LUZ, B. and CROWLEY, J.K. Identification of plant species by using high spatial and spectral resolution thermal infrared (8.0–13.5 µm) imagery. *Remote Sensing of Environment*. 2010, **114**(2), 404-413. DOI: 10.1016/j.rse.2009.09.019.

[29] SABOL, Jr., D.E., GILLESPIE, A.R., ABBOTT, E. and YAMADA, G. Field validation of the ASTER Temperature–Emissivity Separation algorithm. *Remote Sensing of Environment*. 2009, **113**(11), 2328-2344. DOI: 10.1016/j.rse.2009.06.008.

[30] SALISBURY, J.W., WALTER, L.S., VERGO, N., D'ARIA, D.M. *Infrared (2.1-25 um) spectra of minerals*. Baltimore: John Hopkins University Press, 1991. ISBN 0801844398.

[31] SOBRINO, J.A., FRANCH, B., MATTAR, C., JIMÉNEZ-MUÑOZ, J.C. and CORBARI, C. A method to estimate soil moisture from Airborne Hyperspectral Scanner (AHS) and ASTER data: Application to SEN2FLEX and SEN3EXP campaigns. *Remote Sensing of Environment*. 2012, **117**, 415–428. DOI: 10.1016/j.rse.2011.10.018

[32] SOBRINO, J.A., JIMÉNEZ-MUÑOZ, J.C., LABED-NACHBRAND, J. and NERRY, F. Surface emissivity retrieval from Digital Airborne Imaging Spectrometer data. *Journal of Geophysical Research: Atmospheres*. 2002, **107**(D23). DOI: 10.1029/2002JD002197.

[33] SOBRINO, J.A., JIMÉNEZ-MUÑOZ, J.C., ZARCO-TEJADA, P.J., SEPULCRE-CANTÓ, G. and DE MIGUEL, E. Land surface temperature derived from airborne hyperspectral scanner thermal infrared data. *Remote Sensing of Environment*. 2006, **102**(1-2), 99-115. DOI: 10.1016/j.rse.2006.02.001.

[34] SOBRINO, J.A., OLTRA-CARRIÓ, R., JIMÉNEZ-MUÑOZ, J.C., JULIEN, Y., SÒRIA, G., FRANCH, B. and MATTAR, C. Emissivity mapping over urban areas using a classification-based approach: Application to the Dual-use European Security IR Experiment (DESIREX). *International Journal of Applied Earth Observation and Geoinformation*. 2012, **18**, 141–147. DOI: 10.1016/j.jag.2012.01.022.

[35] WANG, H., XIAO, Q., LI, H. and ZHONG, B. Temperature and emissivity separation algorithm for TASI airborne thermal hyperspectral data. **In:** *2011 International Conference on Electronics, Communications and Control (ICECC)*. Ningbo: IEEE, 2011, 1075-1078. DOI: 10.1109/icecc.2011.6066288.

Curriculum vitae
Ing. Marek Pivovarník

e-mail marek.pivovarnik@gmail.com

Education

Doctoral studies 2012 - 2017	**Brno University of Technology** **Faculty of Mechanical Engineering** Applied Mathematics Dissertation: *New Approaches in Airborne Thermal Image Processing for Landscape Assessment.* Supervisor: doc. Ing. Mgr. František Zemek, Ph.D.
Master's degree 2010 - 2012	**Brno University of Technology** **Faculty of Mechanical Engineering** Mathematical Engineering
2011	**Eindhoven University of Technology** Erasmus Programme
Bachelor's degree 2007 - 2010	**Brno University of Technology** **Faculty of Mechanical Engineering** Mathematical Engineering

Work experience

2016 - now	**Freelance iOS developer**
2014	**University of Valencia** Internship
2012 - 2016	**Global Change Research Institute CAS** Processing airborne thermal hyperspectral images